Ocean Engineering 263 (2022) 112343

Contents lists available at ScienceDirect

Ocean Engineering

journal homepage: www.elsevier.com/locate/oceaneng

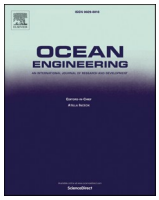

Determination of extreme responses of USFG's equilibrium glide path hovering in ocean current

Usman Nawaz Ahmad [a], Yihan Xing [a,*], Shuaishuai Wang [b]

[a] University of Stavanger, Norway
[b] Norwegian University of Science and Technology, Trondheim, Norway

A B S T R A C T

The UiS subsea-freight glider (USFG) is a state-of-the-art autonomous vessel designed to be an alternative to existing transportation technologies and serve the demands of small-scale fields for CO_2 transportation. Generally, these smaller fields cannot economically justify the costs of large tankers, cargo ships, or underwater pipelines on the seabed, as the transport volume is nominal compared to larger fields. The USFG can travel underwater at an operational depth of 200 m, allowing the glider to carry freight operations without considering ideal weather windows. It can manoeuvre itself underwater by monitoring the flow between the ballast tanks aboard. During the entire mission of the USFG, from capturing to injection locations, it follows a pre-laid saw-tooth path while experiencing transient loads from the ocean current. The extreme surge and heave responses of the USFG are vital for its design. Extreme motion along the surge direction affects the range of the glider (vital for battery design) and the dynamic controller parameters concerning manoeuvrability. For this paper, the averaged conditional exceedance rate (ACER) is employed to scrutinize the extreme motion (surge direction) of the USFG while gliding to a defined depth. This is done when the glider is exposed to an average current velocity of 0.5 m/s and 1.0 m/s. The data used for analysis in this study is obtained from the time-domain simulations carried out on a two-dimensional mathematical model developed in Simulink. The presented ACER method efficiently uses the available data points and accurately predicts the extreme surge responses precisely and accurately. This study can effectively promote the design improvement of the USFG; thus, the safety and economic benefits can be essentially enhanced.

1. Introduction

The UiS subsea-freight glider (USFG), depicted in Fig. 1, is a state-of-the-art sizeable underwater cargo-carrying vessel proposed by Xing (2021). Subsequently, work by Ahmad and Xing (2021) studied the critical controller parameters to design an optimal and robust control for the autonomous gliding capabilities of the USFG. This formed the basis for choosing an ideal controller for the USFG for its gliding capabilities, as highlighted by Ahmad and Xing (2022). Xing et al. (2021a) contended that for an autonomous freight carrying vessel to be economically feasible, the assigned payload should be a minimum of 50% of its volumetric displacement. Xing et al. (2021a) also proposed numerous optimization techniques and innovative design features to reduce the overall weight of the vessel significantly. Founded on these considerations, Ahmad et al. (2022) developed the baseline design of the USFG.

The baseline design of the USFG is a 531-deadweight tonnage (DWT) subsea glider. It is planned to play a pivotal role in the transportation operations for carbon capture and storage (CCS). The glider aims to carry the CO_2 from the capturing facilities to the storage facilities offshore, injecting the CO_2 into the seabed with the aid of wells located at the seabed, as shown in Fig. 2. The USFG travels at an operating depth of 200 m, where waves and wind loads do not affect the critical freight operations. Consequently, the USFG is not weather restricted; owing to its autonomous and submarine capabilities, it can transport CO_2 even in extreme sea conditions compared to conventional tankers.

The USFG can be fully incorporated into the ongoing CCS projects on the Norwegian Continental Shaft (NCS), namely, Snøhvit, Sleipner, and Utgard fields, as shown in Fig. 3. It aims to assist as an auxiliary solution to conventional transport methods such as pipelines and tankers. As for small fields with lower storage volume, the costs of tanker ships and subsea pipelines cannot be commercially justified. Additionally, as considered in Xing et al. (2021b), the cost/ton of carrying CO_2 is anticipated to be more cost-effective than pipelines and tankers. Moreover, the transportation cost is projected to be equivalent to the innovative subsea shuttle tanker (SST) presented by Ma et al. (2021a). With design optimizations, as argued by Jamissen et al. (2022), the USFG can fiscally be an increasingly attractive underwater vessel. The baseline USFG is used for the study in this work; Table 1 highlights the key design features of the USFG.

The USFG can manoeuvre itself freely by operating the ballast tanks

* Corresponding author.
E-mail address: yihan.xing@uis.no (Y. Xing).

https://doi.org/10.1016/j.oceaneng.2022.112343
Received 21 May 2022; Received in revised form 7 August 2022; Accepted 17 August 2022
Available online 30 August 2022

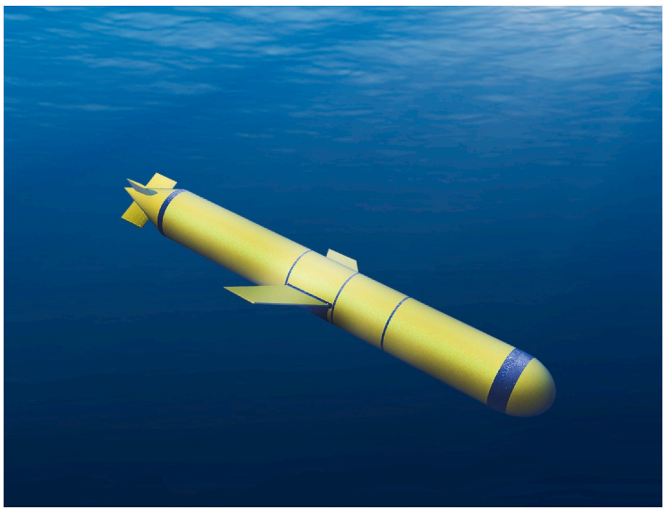

Fig. 1. The UiS subsea-freight glider (USFG).

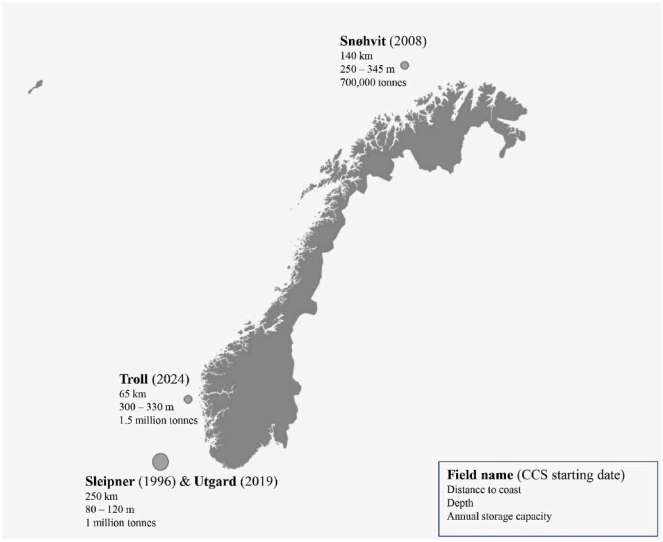

Fig. 3. Sites on NCS for CCS to integrate USFG.

aboard. As depicted in Fig. 4, the pre-planned path or route of the USFG is also known as the equilibrium gliding path (Bahlman et al., 2012). Positive net buoyancy and negative pitch angle are primarily generated by pumping out the ballast water. This allows the vessel to rise with an angle of attack (bow heading up). Consequently, a lift force is produced due to the relative velocity between the incoming seawater and the glider, allowing the glider to move in the required direction. Correspondingly, the glider can return to its primary depth by pumping in the ballast, which generates a negative net buoyant force and positive pitch angle (bow heading down). While moving forward in this saw-tooth pattern, the large hydrofoils are responsible for generating propulsion. This cyclic process is repeated throughout the entire mission of the USFG until it reaches its targeted destination through being exposed to the environmental loads, as highlighted in Fig. 4. The Linear Quadratic Regulator (LQR) is responsible for controlling the motion of the USFG, which is fine-tuned and modelled by Ahmad et al. (2022).

Extreme surge responses are vital considering the design of the USFG. Following a pre-planned path is vital when CO2 is transported from offshore to an onshore field during the mission. This must be done to maximize the travel or operational range of the glider. The path also depends on the extreme surge motion (which can also influence motion in the heave direction). The glider's ability to manoeuvre accurately underwater is of utmost importance for controller design. The controller must cater to the undershoot or overshoot in the surge direction, as depicted in Fig. 4. The goal is to utilize not more than one-fourth of the battery power by following a defined path, which can likely reduce power consumption, as argued by Langebrake (2003). Following the route is of great importance, as this can remedy the problem of limited position tracking of AUVs, as emphasized by Griffiths et al. (Griffiths, 2002). Any deviation from the route must be avoided as it can lead to severe consequences, i.e., loss of vessel control.

In this work, the averaged conditional exceedance rate (ACER) is utilized to study the extreme motion (surge direction) of the USFG during gliding. This is done when the vessel is exposed to an average current velocity of 0.5 m/s and 1.0 m/s. The ACER method is defined by

Table 1
USFG's design characteristics.

Parameter	Value	Unit
Length	50.25	m
Operating depth	200	m
Center of gravity (CoG) $[x_{cg}, y_{cg}, z_{cg}]$	[-0.78, 0.00, 0.40]	m
Weight	1379	tons
CO_2 cargo capacity	518	m^3
Beam	5.5	m
Range	400	km
Center of buoyancy (CoB) $[x_{cb}, y_{cb}, z_{cb}]$	[-1.48, 0.00, 0.00]	m
Wing area	5	m^2

combining two methods: an extrapolation method utilizing tail behaviour and a numerical method that evaluates the extreme value distribution intrinsic to the acquired data. Compared to other extreme value prediction methods, the ACER method is accurate, convenient, and robust. Previously, the ACER design method has been effectively utilized for various applications in the field of marine engineering to evaluate extreme sea states involving current profiles (Yu et al., 2020), waves and wind profiles (Naess and Karpa, 2015; Gaidai et al., 2019a, 2019b), and wave heights (Gaidai et al., 2019a, 2020). Also, for structural applications such as (Xu et al., 2019; Naess and Moan, 2013; Gaidai et al., 2021; Naess and Gaidai, 2008; Naess et al., 2008, 2010; Hui et al., 2019). The glide problem under consideration is highly non-linear.

Consequently, ACER is utilized for this study, as it studies the non-linearities of the system beyond making any generalizations or simplifications with an added advantage of it being Monte Carlo-based. All the data in this study is obtained from the time-domain simulations carried out on a two-dimensional mathematical model design in Simulink, ref Section 2. The ACER method is presented in Section 3. Detailed findings of this work and conclusions are presented in Sections 4 and 5, respectively.

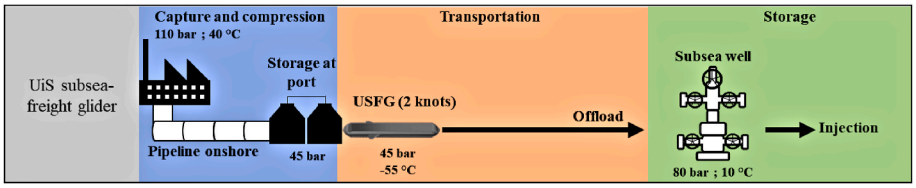

Fig. 2. Usfg in CCS.

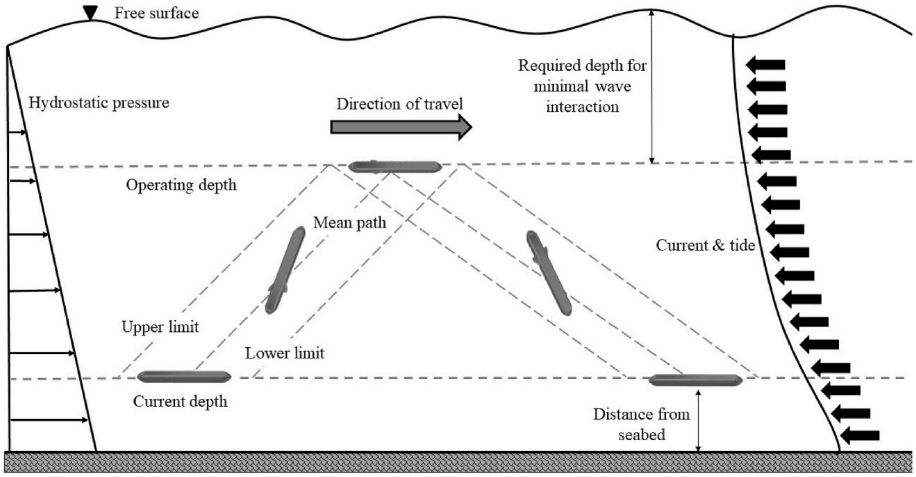

Fig. 4. USFG subjected to environmental loads during equilibrium glides.

2. Two-dimensional mathematical model

MATLAB has been used to capture the dynamics of the USFG by modelling it as blocks or modules representing the vessel's various components. The USFG is represented by a planar multibody model which has been developed in the Simulink environment. The model is presented in this section. The variable step ODE45 Simulink solver uses a relative error tolerance of 10-3 and an absolute error tolerance of 10-6. These error tolerances are strict and will lead to accurate dynamic simulation results.

2.1. Coordinate system

A body-bounded and an earth frame are defined to capture the system dynamics of the USFG fully. The vessel's motion, vector direction, and axis system are presented in Fig. 5 below. The body-bounded frame (O_{bb}, X_{bb}, Y_{bb}, Z_{bb}) is positioned at USFG's centre of gravity (G). The global coordinate system is represented by the origin O_{EB} and the axes X_{EB}, Y_{EB} and Z_{EB}. The buoyancy centre (B) falls directly above the geometric centre to ensure the vessel's stability.

2.2. Simulink layout

The control loop and mathematical model of the USFG designed in Simulink are shown in Fig. 6 and Fig. 7, respectively.

This model was initially developed by Ahmad and Xing (2021) to capture the system dynamics of the USFG during equilibrium gliding

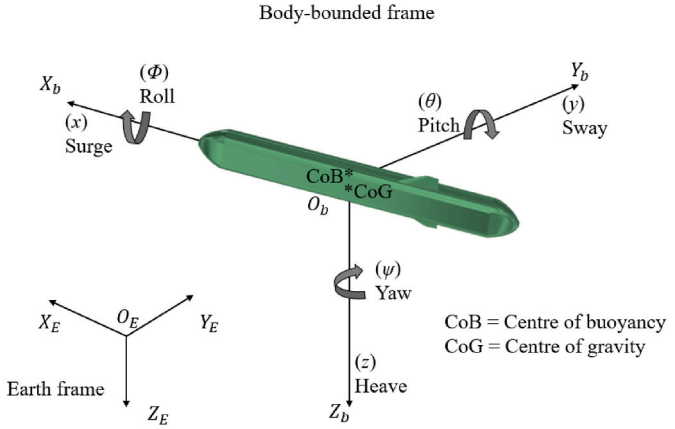

Fig. 5. USFG's axis system.

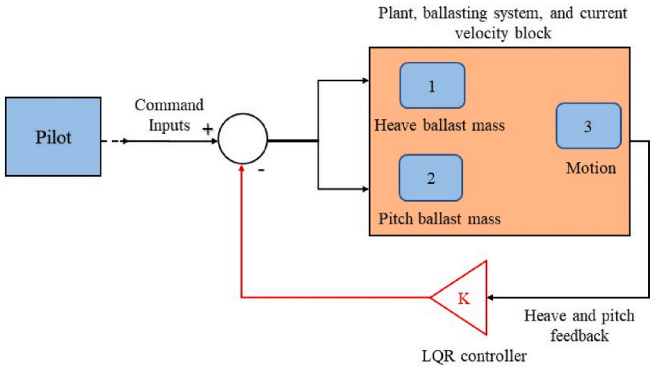

Fig. 6. Control loop for USFG's mathematical model.

while following a pre-planned path. Later, Ahmad and Xing (2022) extended their work to include an LQR-based control for depth and pitch control using a hydrofoil while undergoing loads from the current.

The main modules of the USFG are the following:

- *Plant module/block:* this block represents the USFG in the Simulink environment. It is responsible for executing and solving the equation of motions for the USFG. This is done by considering the effect of hydrofoil and the body's lift and drag forces, hydrostatics of the vessel, and hydrodynamic derivatives.
- *Ballast system module/block:* it is responsible for regulating the mass of the ballast between the tanks aboard the vessel. This block provides actuation to the glider that allows it to manoeuvre in the heave direction with the aid of its hydrofoils, which are responsible for producing the drag and lift forces. Also, the pitching motion of the glider is controlled by this block by varying the ballast water; this allows the glider to pitch forward (bow heading downwards) and vice versa. Further, to limit the volumetric flow rate of the ballast between the tanks, a rate-limiter is also applied in this block. Similarly, the amount of ballast regulated amongst the tanks is also limited by a saturation unit.
- *Current block:* to simulate the response of the USFG in ocean currents, this block is added to generate the current velocities.
- *Control system block:* termed LQR in Fig. 6, this module represents the entire control system for the USFG.
- More details of this model can be found in the work by Ahmad and Xing (Ahmad et al., 2022).

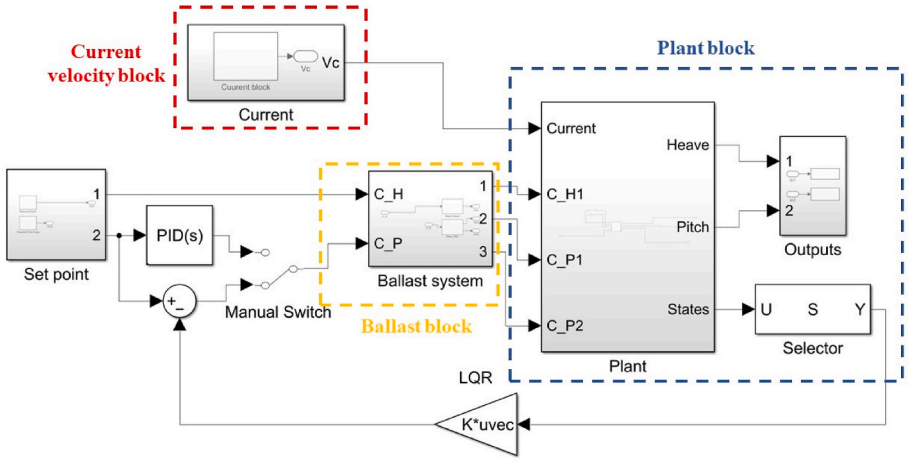

Fig. 7. Simulink design - ballast, current velocity, and plant block.

2.2.1. Plant module/block

This section fully defines the plant module highlighted in Fig. 7. A two-dimensional rigid body is defined to represent the vessel. The body can move freely in three directions or degrees of freedom (*x, z, and q*), representing surge, heave, and pitch, as depicted in Fig. 5.

The equations of motion are stated below:

$$Mg\left(\dot{u}+wq-x_{cg}q^2+z_{cg}\dot{q}\right)=\sum X_e \tag{1}$$

$$Mg\left(\dot{w}-uq-z_{cg}q^2-x_{cg}\dot{q}\right)=\sum Z_e \tag{2}$$

$$I_{zz}\dot{q}+Mgz_{cg}\left(\dot{u}+wq\right)-x_{cg}\left(\dot{w}-uq\right)=\sum Q_e \tag{3}$$

where M is the mass of the USFG, I_{zz} is the moment of inertia in pitch, g is the gravitational acceleration, (x_{cg}, z_{cg}) is the center of gravity and $\sum X_e$, $\sum Z_e, \sum Q_e$ are the sum of external forces in the surge, heave and pitch directions, respectively. The external forces consist of hydrostatic, added mass, lift and drag forces.

The hydrostatic forces are given as follows:

$$X_{HS}=(B-Mg)\sin\theta \tag{4}$$

$$Z_{HS}=(B-Mg)\cos\theta \tag{5}$$

$$M_{HS}=-z_gB\sin\theta-x_gB\cos\theta \tag{6}$$

where X_{HS}, Z_{HS} and M_{HS} are the hydrostatics loads in the surge, heave and pitch directions, respectively, and θ is the Euler angle in pitch which is also the pitch displacement in the present 2D planar model.

No added mass is applied in the surge direction as this is negligible for torpedo-shaped bodies such as the USFG (Ma et al., 2021b). The added mass forces for the heave and pitch directions, Z_A and M_A are calculated as follows:

$$Z_A=C_{A,Z}M\dot{u} \tag{7}$$

$$M_A=C_{A,M}I_{zz}\dot{q} \tag{8}$$

$C_{A,Z}$ and $C_{A,M}$ are the added mass coefficients for the surge and pitch directions, respectively and are defined to be 1.0.

The lift (L_f) and drag (D_f) forces along with the rotational torque (M_T) acting on the body of the USFG are also calculated in this module, which is given by equation (4).

$$\begin{aligned} L_f&=\frac{1}{2}\times L_c\times\delta\times V_s\times V^2\\ D_f&=\frac{1}{2}\times D_c\times\delta\times V_s\times V^2\\ M_T&=-\frac{1}{2}\times C_M\times\delta\times V_s\times q^2 \end{aligned} \tag{9}$$

where δ is the seawater density, V_s is the total submerged volume of the USFG, and V is the total velocity with which the USFG manoeuvres. L_c and D_c are the lift and drag coefficients given by equations (5) and (6), respectively, whereas C_M is the damping moment coefficient whose value is defined as 1000. The C_M value used has been tested using decay tests and is shown to work well for this study. It is noted that this value would need to be obtained via experimental testing for real-life applications.

$$L_c=100\alpha^2+5\alpha \tag{10}$$

$$D_c=30\alpha^2+1.8 \tag{11}$$

These volumetric constants depend on the external flow's approach angle or the angle of attack (α). Further, the coefficients are determined based on the CFD work by Du et al. (2014), which studied a submarine hull of close geometrical similarity.

Similarly, the drag and lift generated by the large hydrofoils are also applied and modelled in this plant model. Ahmad et al. (2022) calculated the reference wing area for the hydrofoils that are incorporated into this module. NACA 4412 airfoil (Tools) geometry is used to model the dynamics of the USFG's wings. External forces and the rotational moment/torque remain the same as equation (4), except for volumetric coefficients. H_L and H_D are the lift and drag forces generated by the hydrofoils, while M_H is the moment. The modified equations for the hydrofoils are given below:

$$\begin{aligned} H_L&=\frac{1}{2}\times L_{ch}\times\delta\times V_s\times V^2\\ H_D&=\frac{1}{2}\times D_{ch}\times\delta\times V_s\times V^2\\ M_H&=-\frac{1}{2}\times C_{Mh}\times\delta\times V_s\times q^2 \end{aligned} \tag{12}$$

whereas L_{ch}, D_{ch}, and C_{Mh} are the modified volumetric coefficients given below.

$$\begin{aligned} L_{ch}&=a\alpha^3+b\alpha^2+c\alpha+d\\ a&=-10\times10^{-5};b=-9\times10^{-4};c=0.114;d=0.4942 \end{aligned} \tag{13}$$

$$D_{ch} = Ae^{(B\alpha)} + Ce^{(D\alpha)}$$
$$A = 2 \times 10^{-3}; B = -0.2093; C = 2.5 \times 10^{-3}; D = 0.1892 \quad (14)$$

$$C_{Mh} = q + w\cos(\alpha u) + r\sin(\alpha u) + t\cos(2\alpha u) + y\sin(2\alpha u)$$
$$q = -0.085; w = -0.026; r = 0.014; t = 0.0076; y = -0.0076 \quad (15)$$
$$u = 0.1595$$

2.2.2. Ballast module/block

The dynamics of the actuating system of the USFG ballast tanks are modelled in this block. It is noted that the model by Ahmad and Xing (2022) utilizes only ballast tanks for propulsion, where the actuator mechanism does not encompass any secondary sources such as thrusters, propellers, or skegs for manoeuvring of USFG. The overall arrangement and placement of all the tanks aboard the USFG are illustrated in Fig. 8. The ballast tanks are the trim and compensation tanks located at the fore and aft of the USFG.

The ballast tanks on the USFG are divided into trim and compensation, responsible for the vessel's stability as they induce neutrally trim and floating conditions. The compensation tanks at the stern and bow provide the vessel with the required trimming moment and ballast mass to attain neutral buoyancy. Moreover, a pair of smaller trim tanks (in volume) located at the same position ensures that the G of the vessel always remains below the B, providing finer alterations. Doing this allows the vessel to maintain a neutral or zero trim state. Also, apart from the ballast tanks, the buoyancy tanks onboard the USFG can enhance the overall stability of the vessel by increasing the ballasting capacity. It is noted that the USFG diving depth (200 m) is much less than traditional gliders (typically a few thousand meters), and therefore, the effect of seawater density change with water depth experienced by USFG is much smaller and has less influence on the glider motion. Therefore, this paper does not consider seawater density differences with water depth.

2.2.3. Current module/block

The first-order Gauss-Markov process (Fossen, 2011) is used to simulate the ocean current. Current velocity U_c, and the incoming current flow angle φ_c is given by equations (11) and (12).

$$\dot{U}_c + \nu_1 U_c = \lambda_1 \quad (16)$$

$$\dot{\varphi}_c + \nu_2 \varphi_c = \lambda_2 \quad (17)$$

To determine the time constants of the Gauss-Markov process, constants ν_1 and ν_2 are used and adhering to Fossen (2011), their magnitude should be a positive value. λ_1 and λ_2 are expressed as Additive White Gaussian Noises (AWGN). To generate a steady current, smaller values of ν_1 and ν_2 are utilized in this analysis, i.e., 1. For producing a fluctuating effect in the current direction and velocity, the noise power is limited to 1/10. The maximum current velocity experienced at the NCS is 1 m/s (Ersdal, 2001), but for this analysis, the design current speed for USFG is reduced to 0.5 m/s.

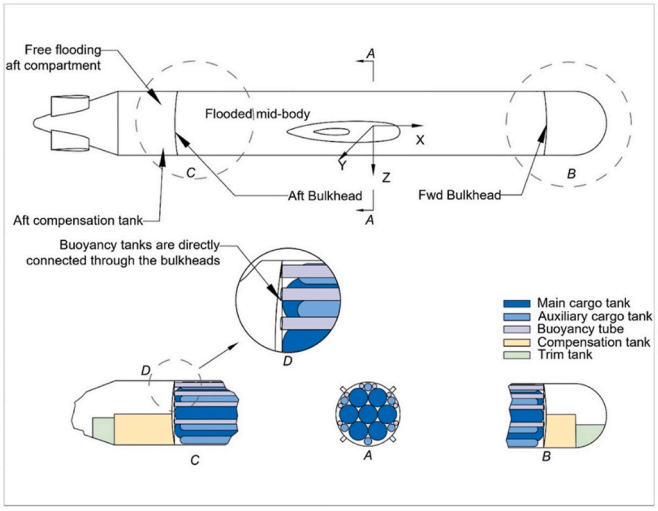

Fig. 8. Tank arrangement of USFG (Ahmad et al., 2022).

Current velocities in heave and surge directions, as expressed in USFG's body frame, are given as:

$$u_{wc} = U_c \cos \varphi_c \quad (18)$$

$$w_{wc} = U_c \sin \varphi_c \quad (19)$$

The velocity of the water in vertical (z) and horizontal (x) directions is given by w_{wc} and u_{wc}, respectively. Below is the incoming relative velocity encountered by the USFG in heave and surge.

$$w = w_{USFG} - w_{wc} \quad (20)$$

$$u = u_{USFG} - u_{wc} \quad (21)$$

where u_{USFG} and w_{USFG} are USFG's velocities in surge and heave.

2.2.4. Control system module/block

Linear quadratic regulator (LQR) type control is applied in this analysis, which controls the vessel's motion in heave and pitch directions. Previously, LQR has been applied to numerous autonomous marine vehicles due to its robust and stable performance. Burlacu et al. (2007) and Bae et al. (BaeShin et al., 2014) used LQR for depth and steering control of marine vehicles, respectively. The LQR-type control utilizes full state feedback to stabilize the system's step responses. For LQR's control strategy, adaptive and optimum gains are fed into the close-loop; this enhances the system's overall response. Gains can be derived from the USFG's state-space equations. For a single input and multiple output system, state-space equations are given in equations (17) and (18) for equations.

$$\frac{dx_{1,2}}{dt} = Jx_{1,2} + Ku_{1,2} \quad (22)$$

$$y_{1,2} = Lx_{1,2} \quad (23)$$

Here $y_{1,2}$ represents the output vector of the system, $u_{1,2}$ and $x_{1,2}$ are the input and state vectors, respectively. While L signifies output matrix, K and J are expressed as input and state matrices correspondingly. These matrices L, K, and J are calculated in the *System linearization* section below.

Actuator effort and system performance are compared and balanced to achieve the ideal and robust controller gain matrix for LQR-type control. The control law implemented in this study is represented by $S = -Gx$; here, G is the optimum gain matrix. The control law aims to decrease the infinite sum of variations from the principal quantities, also known as the quadratic cost function:

$$C = \int_0^\infty \delta x^T N \delta x + \delta u^T M \delta u \, dt \quad (24)$$

Here N and M are weight matrices for the state and energy (actuator effort), respectively; the idea is to adjust the weights of both matrices to obtain a robust system performance efficiently by applying little actuator effort. LQR controller can be tuned by varying the weights (values) of N and M matrices; this is highlighted in section *Controller tunning* below.

2.2.4.1. System linearization. For a front-to-front inflow of ocean current, Ahmad and Xing (2021) investigated that the 38° equilibrium glide path is suitable, which is the targeted analysis for this study. Earlier, Ahmad and Xing (2022) linearized the mathematical model of the USFG at two different glide angles, 30° and 40°. For this work, the model is

linearized at a gliding angle of 38° by using the model linearizer in the Simulink environment. The outputs $[\dot{\theta}; \ddot{x}; \ddot{y}; \ddot{\theta}]$ and inputs $[\theta; \dot{x}; \dot{y}; \dot{\theta}]$ into the system are designed as open-loop and are linearized at a functioning point for a stable current speed of 0.5 m/s. As a result, a 4 by 4 state, 2 by 4 output, and 4 by 1 input matrix are given by equations 20–22.

$$J = \begin{bmatrix} 0 & 0 & 0 & 1 \\ 0.43 & -0.20 & -0.26 & 6 \times 10^{-12} \\ 0.68 & -0.29 & -0.41 & 0 \\ -2 \times 10^{-08} & 1 \times 10^{-09} & 2 \times 10^{-09} & -3 \times 10^{-04} \end{bmatrix} \tag{25}$$

$$K = \begin{bmatrix} 0 \\ -1.58 \times 10^{-12} \\ -8.88 \times 10^{-13} \\ 2.64 \times 10^{-05} \end{bmatrix} \tag{26}$$

$$L = \begin{bmatrix} 0 & 0.79 & -0.61 & 0 \\ 0 & 0.46 & -0.59 & 0 \end{bmatrix} \tag{27}$$

2.2.4.2. Controller tunning. To obtain an optimal response of the USFG during equilibrium gliding, the LQR-type controller is tuned by utilizing the state-space matrices (J and K). The system's dynamics should be entirely explicit to the user to tune the controller efficiently. This can be done by varying the weights or values of the N and M matrices while observing the transient response of the system in retort to the output or performance. Adjusting the weights of the N matrix varies the steady-state error of the output. At the same time, M matrix is utilized to regulate the amount of energy spent on the actuators. N and M matrices are highlighted in equation (23).

$$N = \begin{bmatrix} 0 \\ 0 \\ 0 \\ 10^{3} \end{bmatrix} \tag{28}$$

$$M = \begin{bmatrix} 10^{-2} \end{bmatrix}$$

To have an enhanced response for pitch motion, the acceleration coefficient, i.e., 10^3 is weighted heavily. This yields a gain matrix G given below.

$$G = \begin{bmatrix} -5.3 \times 10^{-10} & 2.4 \times 10^{-10} & 3.2 \times 10^{-10} & 2.6 \end{bmatrix} \tag{29}$$

3. The average conditional exceedance rate (ACER) design method

$H(t)$ represents the long-drawn-out global or total response of the USFG during gliding, measured for a timespan $(0,\ S)$. The process $H(t)$ measurements are given by $H_1,\ldots,H_N$, which are measured at a distinct timespan $s_1,\ldots,s_N$ in $(0,S)$. This aids in approximating the distribution function of the extreme responses or values $E_N = \max\ \{X_j : j = 1,\ldots,N\}$. Later this can be used to acquire the cumulative density function (CDF), $P(\zeta) = \text{Prob}(E_N \le \zeta)$. This is done to have an approximate CDF for large-scale output ζ values. Hence, the following functions are introduced for this study, having random nature.

$$Q_{kj}(\zeta) = 1\{H_j > \zeta, H_{j-1} \le \zeta, \ldots, H_{j-k+1} \le \zeta\},\ j = k, \ldots, N,\ k = 2,\ 3, \ldots \tag{25}$$

in addition

$$R_{kj}(\zeta) = 1\{H_j > \zeta, H_{j-1} \le \zeta, \ldots, H_{j-k+1} \le \zeta\},\ j = k, \ldots, N,\ k = 2,\ 3, \ldots \tag{26}$$

Here $1\{\mathscr{K}\} = 1$ if $\mathscr{K}$ is correct or true, whereas it is 0 otherwise. As highlighted in Naess et al. (Naess and Moan, 2013) (Naess and Gaidai, 2008) (Naess et al., 2010) (Naess et al., 2008):

$$P_k(\zeta) \approx \exp\ \left(-\sum_{j=k}^{N} \frac{\mathbb{E}[Q_{kj}(\zeta)]}{\mathbb{E}[R_{kj}(\zeta)]} \right) \approx \exp\ \left(-\sum_{j=k}^{N} \mathbb{E}[Q_{kj}(\zeta)] \right),\ \zeta \to \infty \tag{1}$$

where $\mathbb{E}$ is the expectation operator. To render $\mathbb{E}[Q_{kj}(\zeta)]$ to a constant term, the logged time series is separated into K successive (transient) blocks or modules. So that for adequately huge values of ζ, $\sum_{j\in B_i} \mathbb{E}[Q_{kj}(\zeta)] \approx \sum_{j\in B_i} q_{kj}(\zeta)$. Consequently, resulting in $\sum_{j=k}^{N} \mathbb{E}[Q_{kj}(\zeta)] \approx \sum_{j=k}^{N} q_{kj}(\zeta)$. For the recorded time series, $q_{kj}(\zeta)$ represents the realized values of $Q_{kj}(\zeta)$, while B_i depicts the group of indices for the module with the number i; through $i = 1,\ldots,K$. Subsequently, we have the following relation for the given stationary process:

$$P_k(\zeta) \approx \exp\ \ (-(N-k+1)\widehat{\xi}_k(\zeta)) \tag{2}$$

where,

$$\widehat{\xi}_k(\zeta) = \frac{1}{N-k+1} \sum_{j=k}^{N} q_{kj}(\zeta) \tag{3}$$

To approximate the short-term or transient values by utilizing the detected values of $q_{kj}(\zeta)$ functions, an assumption of ergodicity is employed for every transient part of the logged time series. By examining the empirical probability distribution of $l = 1,..,L$ sea current states have probabilities p_l, so that $\sum_{l=1}^{L} p_l = 1$, an alternate method of expressing the non-transient extreme value distribution, equation (28), can be attained.

Accordingly, the long-term/non-transient ACER function having an order of magnitude k is given by:

$$ACER_k(\zeta) \equiv \sum_{l=1}^{L} \widehat{\xi}_k(\zeta, l) p_l \tag{4}$$

whereas $\widehat{\xi}_k(\zeta, l)$ is limited to an exact sea-state having a number L, which is the same as in equation (29). Founded on the ACER function having an order k, the non-transient extreme value distribution of $E(S)$ can be expressed as:

$$P(\zeta) \approx \exp(-D \times ACER_k(\zeta)) \tag{5}$$

This can also be seen in Naess et al. (Naess and Moan, 2013) (Naess and Gaidai, 2008) (Naess et al., 2010) (Naess et al., 2008). $\text{ACER}_k(\zeta)$ represents the long-term/non-transient observed ACER function having an order of magnitude k with $k \ll D$. where D specifies the overall size of data points from the observed frequency distribution that is utilized to estimate the ACER functions. These are the extreme or output values from the gauged time record.

$ACER_k(\zeta)$ is observed to converge quickly with increasing values of k; this also enhances the accuracy of equation (31), also argued in (Naess and Moan, 2013) (Naess and Gaidai, 2008) (Naess et al., 2010) (Naess et al., 2008). By increasing the processing level k, the data clustering effects (narrow-banded components of the output) can be catered to in the analysis. This enhances the accuracy of the projected extreme values, thus avoiding unstable or impractical design values.

For higher output/response values of ζ, the behaviour in the tail is relatively consistent or steady for the $ACER_k$ represented as functions. Moreover, for $\zeta \ge \zeta_0$, the tail performs intimately like $exp\{-q(\zeta + r)^u + v\}$ with q, r, u, v representing the appropriate constant values.

Log-level optimization can be performed by minimizing the error function W by considering q_k, r_k, u_k, v_k as the input arguments.

$$F(q_k, r_k, u_k, v_k) = \int_{\zeta_0}^{\zeta_1} \alpha(\zeta)\{ln(ACER_k(\zeta)) - v_k + (q_k\zeta + r_k)^{u_k}\}^2 d\zeta,\ \zeta \ge \zeta_0 \tag{6}$$

The highest output value that permits the calculation of the

confidence interval is represented by ζ_1, it is also known as the designed limit for cut-off. Where α is the weight function represented as $\alpha(\zeta) = \{lnC^{+}(\zeta) - lnC^{-}(\zeta)\}^{-2}$ with $(C^{-}(\zeta), C^{+}(\zeta))$ depicting the 95% confidence interval (CI), analytically approximated from the recorded data. The comprehensive optimization process for the parameters q_k, r_k, u_k, v_k is highlighted and discussed in Naess et al. (Naess and Moan, 2013) (Naess and Gaidai, 2008) (Naess et al., 2010) (Naess et al., 2008).

4. Results and discussions

Current velocities of 0.5 m/s and 1 m/s are utilized for this analysis. The average current velocity of 0.5 m/s is used as a targeted base-case for USFG, which forms the basis of USFG manoeuvrability in a head-on current of 1 m/s. A total of 60, 750-s cases are collectively simulated for this study.

A tuning study is done for various cases of LQR gains. This is done to enhance the overall step-performance of the control system. The tunning cases are highlighted in Table 2.

Case-4 PD depicts the proportional-derivative (PD) type control used for the collation analysis for the rise time analysis. Depth sensitivity analysis is also presented as a case study in this paper, highlighting the changes in USFG's response in heave for varying operational depth.

This work extends the method for predicting the extreme surge responses of the USFG during its single cycle of equilibrium glide. These responses are estimated while the USFG targets to attain a pre-defined pitch angle and operating depth while manoeuvring in the ocean current. This paper's numeric data is obtained from explicit mathematical simulations based on the Simulink model discussed in Section 2. Section 3 presents the novel ACER method. The presented ACER method utilizes the available data efficiently and predicts the extreme surge responses precisely and accurately. It is established that the ACER method efficiently integrates the environmental disturbances while providing robust and accurate response values, given the exact numerical data.

To minimize the power consumption and any accidental damages during the mission, this well-defined approach can serve as an input to the design and analysis stage of USFG. This can assist in providing optimal and robust control parameters for the glider during operation.

4.1. Performance analysis of the control system

A systematic tuning study is performed in this section. Here, the minus sign indicates that the glider is descending (bow heading down). The desired response is to attain a pitch angle of -38°.

USFG is tuned with different controller gains to study the dynamic response of the glider. The system's response time, stability, and robustness are studied and discussed here. Various tuning cases are highlighted in Table 2.

Fig. 9 depicts the three-pitch responses of the USFG simulated for different cases of the LQR controller. For Case-1 LQR, the steady-state error is the minimum, as shown in Fig. 9. Here the N matrix is penalized heavily in this case which cuts down the system's response time (1700 s) drastically, compelling it to maintain the commanded pitch angle. Moreover, the system is most stable for these gains, as it doesn't experience any oscillations in the output response.

Case-2 LQR depicts an oscillating response as the system minimizes the steady-state error. This increases the response time of the glider (>10000 s). This does not represent the ideal controller gains because

Table 2
Gains for tuning sensitivity study.

Cases	Gains		
Case-1 LQR	$N =$ diag $(0,0,0,10^{3})$	$M =$ diag (10^{-2})	
Case-2 LQR	$N =$ diag $(0,0,0,10^{1})$	$M =$ diag (10^{-2})	
Case-3 LQR	$N =$ diag $(0,0,0,10^{3})$	$M =$ diag (10^{-4})	
Case-4 PID	$P = 102$	$I = 0.18$	$D = 12881$

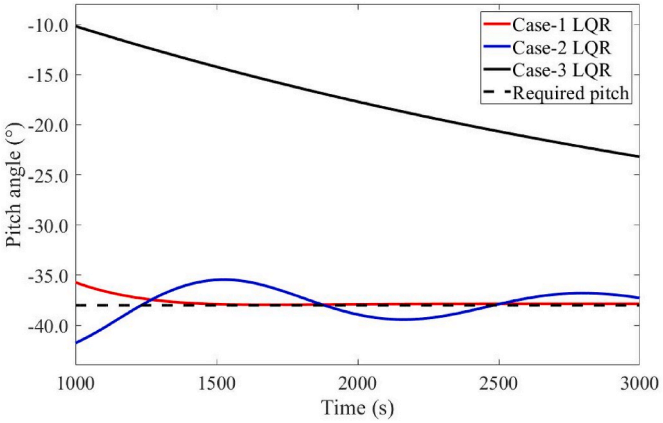

Fig. 9. Pitch responses for LQR tuning.

the system's stability is compromised due to the large variations in the output values. Moreover, the controller spends excessive effort and energy compensating for over-shoot and under-shoot in each successive cycle: as the cost of N matrix is reduced.

As for the last scenario, Case-3 LQR, the M matrix cost is reduced to 10^{-4}. Doing this allows the controller to overcompensate the output pitch response, which increases the response time (>17000 s). Therefore, these LQR gains are not robust and practical for USFG's surge control application as they increase the settling time of the output response.

Fig. 10 highlights the variation of the control parameters, i.e., ballast mass of secondary tanks, for various tuning studies of the LQR controller. These simulations are limited to a 150-s response to obtain a holistic understanding of the entire control process. Case 1 shows minimal variations in the regulated ballast compared to Case 2 and 3, making the glider stable and robust while using these LQR gains.

To measure the robustness of the controller, a settling-time study is framed for different controllers used in this analysis. As depicted in Fig. 11Fig. 10, the glider is allowed initially to attain a diving angle of -15° (bow heading down); afterwards, it is commanded to achieve a $+15^{\circ}$ (bow heading up). This analysis is designed to tackle the unexpected changes in operating conditions of the USFG during its mission. Due to the sluggish response, the Case-3 gains for the LQR-type control are not utilized in this study.

As highlighted in Fig. 11 Fig. 10, the PID controller has the minimum settling time among the controllers. This changes from 250 s for Case-4-PID to 500 s and 800 s for Case-2 LQR and Case-1 LQR, respectively. Consequently, Case-2 LQR and Case-4 PID experience oscillations in

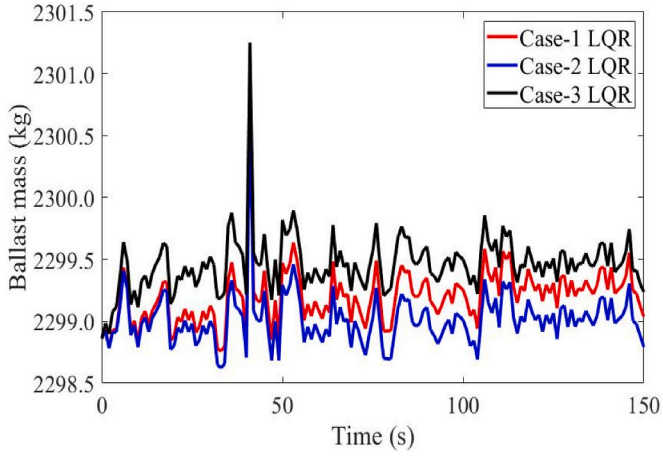

Fig. 10. Ballast mass variation for LQR tuning cases.

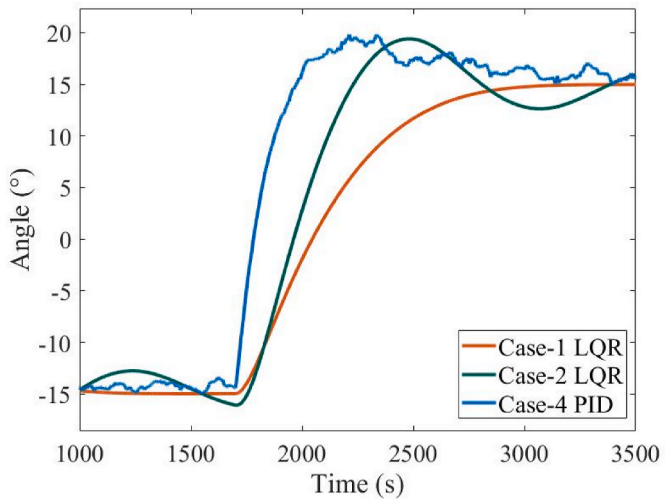

Fig. 11. Settling times for various tuning gains.

their final output response as they are not robust enough to mitigate the noise induced by the ocean current. On the contrary, Case-1 LQR results in a stable and noise-free response at the expense of significant settling times.

Overall, tuning gains for Case-1 LQR are preferred for this analysis as they yield a minimum error in the output without inducing any fluctuations in the system. Further, these weights are also preferred for their minimum expense of actuator effort. They are also utilized for depth sensitivity analysis and univariate extreme response analysis.

4.2. Depth sensitivity analysis

A depth sensitivity study is performed for the USFG to observe the system's responsiveness to changes in operating depths. The USFG is designed for an operating depth of 200 m, as defined by Ahmad et al. (2022) while travelling at an optimal gliding angle of 38°, as argued by Graver (2005). While doing so, the glider covers a total distance of 256 m in the surge direction.

This section studies the changes in surge motion for the variable functional depth of the glider. For each functional depth, 200, 300, and 400 m, the distance covered by the glider is measured and compared against the actual distance. The study aims to observe and mitigate the steady-state error if any in the surge motion.

The 750-s responses for 20 realizations of this study are depicted in Fig. 12. For each case, the distances covered by the USFG are different, which are highlighted in Table 3, along with respective errors.

As depicted in Table 3, the percentage error between the required surge motion values and the desired values is less than 0.4% for all the cases. So, the surge response for variable depths is acceptable within the defined error. This means that additional measures, i.e., increasing ballast fraction or propeller, are not needed in this case. The controller specifications presented in this work can tackle changes in operating conditions while catering to any depth changes throughout the entire mission of the USFG.

4.3. Extreme response prediction: univariate surge analysis

This section highlights the arithmetic results produced by univariate analysis, i.e. ACER1D, for the surge responses for the USFG (Naess and Moan, 2013) (Naess and Gaidai, 2008) (Naess et al., 2010) (Naess et al., 2008). For a safe, robust, and reliable design of the USFG, accurate estimation of extreme surge responses is vital. Fig. 13 depicts the

Table 3
Average errors for depth sensitivity analysis.

Cases	Desired distance (m)	Average measured distance (m)	Percentage error (%)
200 m	256	257	0.391
300 m	384	383	0.260
400 m	512	511	0.195

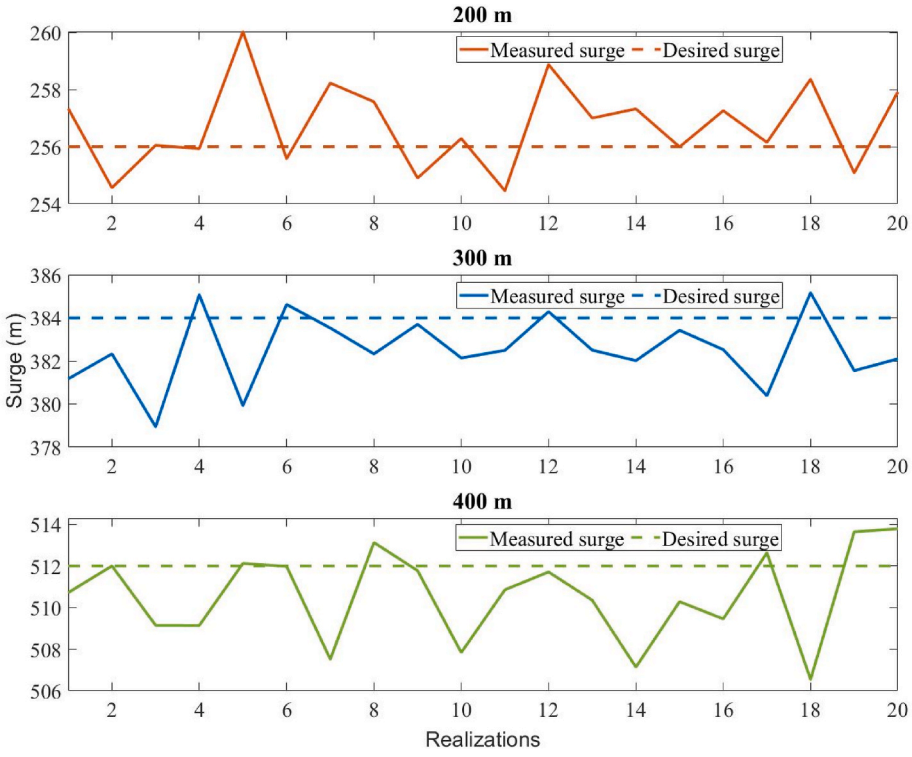

Fig. 12. Simulated responses for 20 surge realizations.

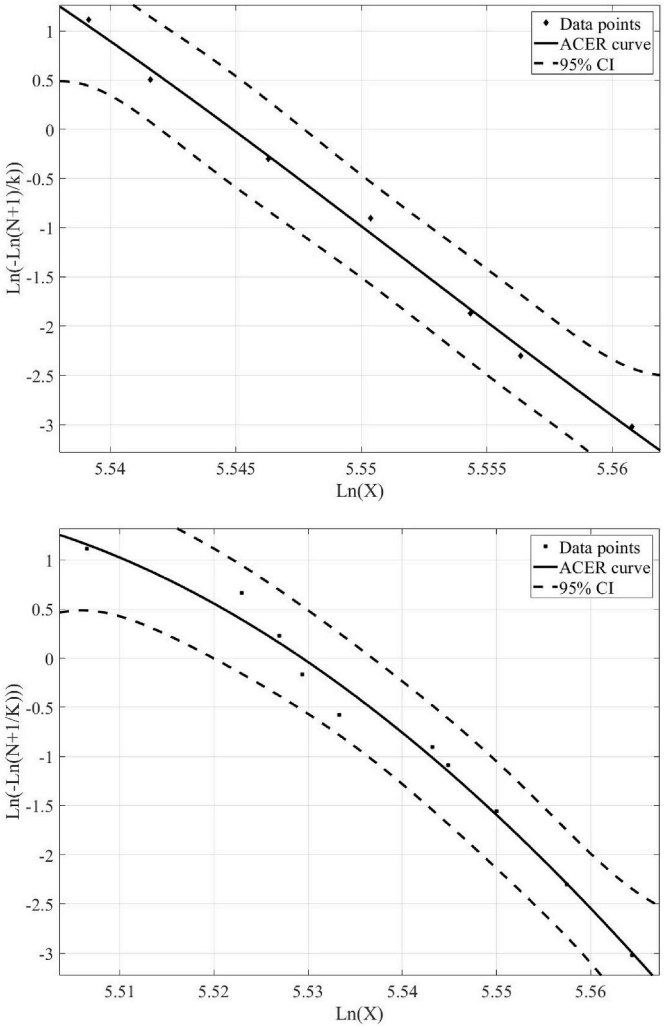

Fig. 13. ACER 1D extreme surge responses in log-scale. Upper: with a current velocity of 0.5 m/s; Lower: with a current velocity of 1.0 m/s.

univariate response for surge and a 95% confidence interval indicated by the dotted lines. Results for several return periods are shown in Table 4; the preferred return periods serve as an example. The Gumbel plot for the surge output is shown in Fig. 14. The fitted curve is extrapolated to represent higher return periods, i.e., 5-year and 10-year. The estimated values given in Fig. 14 can be collated with the ones in Fig. 13 (Lower). While both methods estimate a 3-month return period surge of about 290 m (1.0 m/s case), it is observed that the Gumbel data points from the 20 simulations do not accurately fit a straight curve. Comparable behaviour is observed for all the return periods presented in Table 4. This indicates that the studied data points have not established the asymptotic generalized extreme value (GEV) condition. Additionally, the ACER 95% CI is noticeably narrower than the 95% CI projected

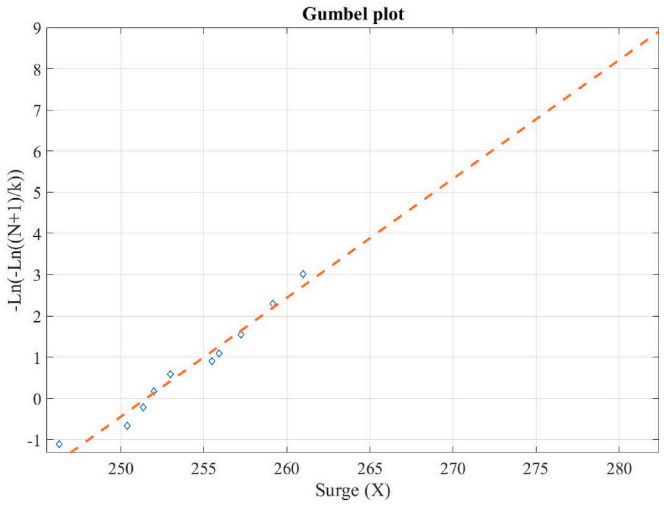

Fig. 14. Gumbel plot for surge, dashed line specifies extrapolation toward a return period of 10-year. 20,750-s simulated responses. Current velocity of 1.0 m/s.

by the Gumbel plot. This is a distinct benefit of utilizing the advanced ACER method for extreme value prediction.

For all the return periods, the extreme surge responses are, in general, more significant than the desired distance (256 m). For instance, for a return period of 5-Year, the extreme values are 1.1–1.2 times higher than the anticipated distance. To compensate for this overshoot, an observer can be employed to the Simulink model that can ensure that the glider follows the path accurately. The difference in the predicted extreme surge values for all the return periods is minimal while moving from left to right in Table 4. For 0.5 m/s current velocity, an alteration of 3 m is observed between 3-Months and 5-Year return periods for both ACER and Gumbel methods. Similar behaviour is also detected for 1.0 m/s current velocity, where a variation of 6 m is realized for both methods.

Table 4 presents the surge output response of the USFG in meters for 5 return periods, i.e., 3-months, 6-months 1-year, 2-year, and 5-year. The Gumbel fit fails to provide accurate and precise estimations in contrast to the 95% CI band predicted by the ACER method.

5. Conclusions

The USFG is a pioneering subsea-freight transportation vessel in its initial design and development phases. The vessel presents numerous exciting development and research challenges to be resolved. The ability of the glider to conserve energy and travel considerable distances during the mission is exceptionally vital for the battery design and the economic feasibility of the USFG. The Simulink model for the USFG is presented in the first part of the work. Numerical modelling is utilized to capture the dynamics of the vessel. The main blocks of the USFG (Plant, Ballast system, Current, and Control system modules) are presented briefly. This paper proposed utilizing the state-of-the-art average conditional

Table 4
Surge response (meters) predictions for several return periods.

Current velocity	Method	3-Months	6-Months	1-Year	2-Year	5-Year
0.5 m/s	**ACER**	270.62 (245.01,307.87)	270.80 (245.18,308.07)	271.25 (245.58,308.58)	271.93 (246.20,309.36)	273.04 (247.20,310.62)
	95% CI					
	Gumbel	270.29 (203.77,317.27)	270.46 (203.90,317.47)	270.89 (204.23,317.98)	271.54 (204.72,318.74)	272.58 (205.50,319.96)
	95% CI					
1.0 m/s	**ACER**	290.99 (231.29,348.60)	291.49 (231.69,349.20)	292.76 (232.70,350.72)	294.68 (234.22,353.02)	297.82 (236.72,356.79)
	95% CI					
	Gumbel	288.49 (218.32,432.51)	288.93 (218.65,433.17)	290.03 (219.48,434.81)	291.69 (220.74,437.30)	294.37 (222.77,441.32)
	95% CI					

exceedance rate (ACER) design method to study the extreme surge responses (offset from the pre-planned surge motion also influences the heave motion of the vessel) while manoeuvring in ocean current during the mission. The surge responses are studied in only the half cycle of the glide, as indicated in Fig. 4. Knowledge of extreme responses of the USFG is vital as it gives the maximum range and depth, which governs the controller gains for motion control and hydrostatic pressure loads, respectively.

Settling and response times are significant for Case-2 LQR and Case-3 LQR, making them impractical for controlling pitching motion. Whereas for Case-1, it was observed that these gains are quite efficient and robust as studied performance analysis of the control system. Furthermore, the PID controller utilized in this study yields a rapid response with fluctuations. This is not suitable as it renders the system unstable. Finally, the tunning gains of Case-1 LQR were preferred owing to small steady-state errors in the response.

From the depth sensitivity analysis, it was concluded that no secondary source of propulsion is needed for USFG. For various operating depths, the maximum error in the output response was about 0.4%, highlighting LQR's tremendous ability in path following.

It is observed that the extreme surge responses for all the return periods are higher, around 1.1 to 1.2 times than the mathematical 750-s response. This specifies that an observer, commonly Luenberger Observer (Luenberger, 1971), can be integrated into the mathematical model of the USFG to ensure path-following even for extreme surge responses, such as depicted in Table 4.

The method proposed in this work enables the USFG design to be matured further. It also contributes to optimizing dynamic vessel parameters and minimizing probable damage to the glider. For future work, the proposed approach can also be applied to the complete equilibrium gliding path (1 complete cycle with turning motion) of the USFG, as presented by Ahmad and Xing (2021). Lastly, the work presented in this paper can be extended to modelling the 3D motion control of the USFG. 3D motion control will involve extensive use of skegs at the aft to induce vessel turning.

CRediT authorship contribution statement

Usman Nawaz Ahmad: Conceptualization, Writing, Conceptualization, Method, Analysis, Discussion. **Yihan Xing:** Conceptualization, Conceptualization, Method, Analysis, Discussion, Funding, Review. **Shuaishuai Wang:** Analysis, Discussion, Review.

Declaration of competing interest

The authors declare that they have no known competing financial interests or personal relationships that could have appeared to influence the work reported in this paper.

Data availability

Data will be made available on request.

References

Ahmad, U., Xing, Y., 2021. A 2D model for the study of equilibrium glide paths of UiS Subsea Freight-Glider. IOP Conf. Ser. Mater. Sci. Eng. 1201 (1), 012022.

Ahmad, U., Xing, Y., 2022. UiS subsea freight glider: controller design and analysis. Int. Conf. Offshore Mech. Arctic Eng. (in print).

Ahmad, U., Xing, Y., Ma, Y., 2022. UiS subsea-freight glider: a large buoyancy-driven autonomous cargo glider. J. Offshore Mech. Arctic Eng. *(Under Review)*.

Bae Shin, S.B., Kwon, D.H., Joo, S.T., G, M., 2014. An LQR controller for autonomous underwater vehicle. J. Inst. Contr. Robot. Syst. 20 (2), 132–137.

Bahlman, J.W., Swartz, S.M., Riskin, D.K., Breuer, K.S., 2012. Glide performance and aerodynamics of non-equilibrium glides in northern flying squirrels (Glaucomys sabrinus). J. R. Soc. Interface 10 (80). https://doi.org/10.1098/rsif.2012.0794, 20120794-20120794.

Burlacu, P., Dobref, V., Badara, N., Tarabuta, O., 2007. A LQR controller for an AUV depth control. Ann. DAAAM Proc. 125–127.

Du, X., Wang, H., Hao, C., Li, X., 2014. Analysis of hydrodynamic characteristics of unmanned underwater vehicle moving close to the sea bottom. Defence Technol. 10, 76–81.

Ersdal, G., 2001. An Overview of Ocean Currents with Emphasis on Currents on the Norwegian Continental Shelf. Norwegian Petroleum Directorate.

Fossen, T.I., 2011. Handbook of Marine Craft Hydrodynamics and Motion Control. John Wiley & Sons.

Gaidai, O., Naess, A., Xu, X., Cheng, Y., 2019a. Improving extreme wind speed prediction based on a short data sample, using a highly correlated long data sample. J. Wind Eng. Ind. Aerod. 188, 102–109.

Gaidai, O., Naess, A., Karpa, O., Xu, X., Cheng, Y., Ye, R., 2019b. Improving extreme wind speed prediction for North Sea offshore oil and gas fields. Appl. Ocean Res. 88, 63–70.

Gaidai, O., Xu, X., Wang, J., Ye, R., Cheng, Y., Karpa, O., 2020. SEM-REV offshore energy site wind-wave bivariate statistics by hindcast. Renew. Energy 156, 689–695.

Gaidai, O., Xu, X., Naess, A., Cheng, Y., Ye, R., Wang, J., 2021. Bivariate statistics of wind farm support vessel motions while docking. Ships Offshore Struct. 16 (2), 135–143.

Graver, J.G., 2005. Underwater Gliders: Dynamics, Control and Design.

Griffiths, G., 2002. Technology and Applications of Autonomous Underwater Vehicles, vol. 2. CRC Press.

Hui, G., Gaidai, O., Naess, A., Storhaug, G., Xu, X., 2019. Improving container ship panel stress prediction, based on another highly correlated panel stress measurement. Mar. Struct. 64, 138–145.

Jamissen, P.L., Ma, Y., Xing, Y.H., 2022. Probabilistic Design of Ring-Stiffened Cylindrical Hull Structures Applied on Large Cargo Submarines, under Review in International Conference on Ocean, Offshore and Arctic Engineering.

Langebrake, L.C., 2003. AUV Sensors for Marine Research. *Technology and Applications of Autonomous Underwater Vehicles*, pp. 245–277.

Luenberger, D., 1971. An introduction to observers. IEEE Trans. Automat. Control 16 (6), 596–602.

Ma, Y., Xing, Y., Ong, M.C., Hemmingsen, T., 2021a. Baseline design of a subsea shuttle tanker system for liquid carbon dioxide transportation. J. Open Eng. 240, 109891.

Ma, Y., Sui, D., Xing, Y., Ong, M.C., Hemmingsen, T.H., 2021b. Depth control modelling and analysis of a subsea shuttle tanker. In: Proceedings of the ASME 2021 40th International Conference on Ocean, Offshore and Arctic Engineering. June 21-30, 2021, Virtual, Online.

Naess, A., Gaidai, O., 2008. Monte Carlo methods for estimating the extreme response of dynamical systems. J. Eng. Mech. 134 (8), 628–636.

Naess, A., Karpa, O., 2015. Statistics of extreme wind speeds and wave heights by the bivariate ACER method. J. Offshore Mech. Arctic Eng. 137 (2).

Naess, A., Moan, T., 2013. Stochastic Dynamics of Marine Structures. Cambridge University Press.

Naess, A., Stansberg, C., Gaidai, O., Baarholm, R., 2008. Statistics of extreme events in airgap measurements. In: International Conference on Offshore Mechanics and Arctic Engineering.

Naess, A., Gaidai, O., Batsevych, O., 2010. Prediction of extreme response statistics of narrow-band random vibrations. J. Eng. Mech. 136 (3), 290–298.

Tools, A. NACA 4412 (naca4412-il). http://airfoiltools.com/airfoil/details?airfoil=naca4412-il.

Xing, Y., 2021. A conceptual large autonomous subsea freight-glider for liquid CO2 transportation. Int. Conf. Offshore Mech. Arctic Eng. 85161. V006T06A052.

Xing, Y., Ong, M.C., Hemmingsen, T., Ellingsen, K.E., Reinås, L., 2021a. Design considerations of a subsea shuttle tanker system for liquid carbon dioxide transportation. J. Offshore Mech. Arctic Eng. 143 (4).

Xing, Y., Santoso, T.A.D., Ma, Y., 2021b. Technical–economic feasibility analysis of subsea shuttle tanker. J. Mar. Sci. Eng. 10 (1), 20.

Xu, X., Gaidai, O., Naess, A., Sahoo, P., 2019. Improving the prediction of extreme FPSO hawser tension, using another highly correlated hawser tension with a longer time record. Appl. Ocean Res. 88, 89–98.

Yu, S., Wu, W., Xie, B., Wang, S., Naess, A., 2020. Extreme value prediction of current profiles in the South China Sea based on EOFs and the ACER method. Appl. Ocean Res. 105, 102408.